Optical and electronic properties enhancement via chalcogenides: Promising materials for DSSC applications

Geradius Deogratias (dgeradius@udsm.ac.tz)
University of Dar es Salaam
Ohoud S. Al–Qurashi
University of Jeddah
Nuha Wazzan
King Abdulaziz University

Research Article

Keywords: Chalcogen, DFT, Electronegativity, Heteroatom, Sensitizer

Posted Date: September 28th, 2022

DOI: https://doi.org/10.21203/rs.3.rs-2078607/v1

Additional Declarations: No competing interests reported.

Version of Record: A version of this preprint was published at Journal of Molecular Modeling on March 6th, 2023. See the published version at https://doi.org/10.1007/s00894-023-05472-0.

Abstract

Comparatively, sensitizers featuring the chalcogen family are less heavily investigated despite their known electronic properties in metal-based materials. In this work, an array of optoelectronic properties is reported using quantum chemical methods. Red-shifted bands within the UV − vis absorption spectrum with absorption maxima > 500 nm in the order of increasing chalcogenides atomic size were observed. There is a monotonic down-shift in the LUMO and ESOP energy consistent with atomic orbital energies (p orbitals) which increases down the group O 2p, S 3p, Se 4p toTe 5p. The excited-state lifetime and free energies of charge injection follow the decreasing order of chalcogenides electronegativity. Adsorption energies of dyes on TiO_2 anatase (101) are in the range of − 0.08 to − 0.77 eV. Based on evaluated properties, selenium and tellurium-based materials hold promise for their futuristic device applications; therefore, this work motivates continued investigation of the chalcogenides sensitizers and their application.

Introduction

Solar energy remains the most favored and promising among renewable energy sources, about ∼3.8 million exajoules are radiated annually, which is 10,000 times the current global demand [1]. The development of techno-economic feasible systems for harvesting and storage of solar energy remains to be the subject of interest. Owing to their advantageous characteristics such as relatively high efficiency, low energy payback time, lightweight, and good performance even under diffuse light [2], dye-sensitized solar cells (DSSCs) present huge potential to revolutionize the energy sector. DSSCs were recently integrated into wearable self − powered energy electronics [3–6] and facilely woven into smart textiles [7]. Despite the recent progress recorded by DSSCs, their power conversion efficiencies are not high enough to compete with the dominant crystalline silicon solar cells.

Following the pioneering work of Grätzel et al in 1991 where power conversion efficiency (PCE) of ∼8% and ∼12% were achieved in simulated solar light and diffuse daylight, respectively, using Ru-based N749 dye and TiO_2 photoanode [5]; many investigations are underway to improve the performance of DSSCs. The current performance of lab-scale DSSCs has reached ∼12–17% [8, 9].

Interestingly, appropriate functionalization of sensitizers may result in the improvement in the optoelectronic characteristics and eventually result in enhanced PCE. Depending on the purpose structural units such as donor (D), π − linkers/bridges, and acceptor (A) can be varied. When variation in structural units is performed the intentions are not limited to widening the absorption bands, increasing light-harvesting efficiency, or improving molecular stability when the dye interacts with the TiO_2 semiconductor. For example, following their remarkable intrinsic properties such as rapid intersystem crossing (ISC), oligothiophenes have been employed as π − linkers in DSSCs materials [10]. The ISC property is vital as it leads to extremely high triplet quantum yields [11–13]. Reports show that the *trans* − conformer of the polythiophene bridges are stable when compared to the *cis* − counterpart and the ultrafast ISC takes place from the first excited singlet state [10]. The torsional motion around the flexible

inter − ring bonds is responsible for the relaxation processes of thiophene oligomers after photoexcitation [14]. A systematic comparison of the optoelectronic properties and their performance for dyes with or without additional auxiliary π − linkers (dithiophene) in the dye's skeleton was carried out by Zhu and co-workers [15]. The overall PCE of ∼8% was recorded for dithiophene-containing molecules; the recorded PCE was found to be ∼1.4 times that of the dye without dithiophene. While chalcogens are ubiquitous for metal-based optoelectronic materials such as CdX [16, 17], CuX [18, 19], CoX [20], ZnX [17, 21, 22] etcetera for X = O, S, Se and Te, heteroatom permutations among chalcogens remain quite poorly explored in the field of DSSCs.

In our recent works, we have demonstrated that the optoelectronic properties of sensitizers containing heavier chalcogens (Se and Te) far surpass those of S-containing sensitizers [23–25]. Motivated by the observed high PCE (8.15%) for dithiophene-containing molecules and superior optoelectronic characteristics for heavier chalcogenides [15, 23–25], it is also of interest to explore a complete series of chalcogenides (O, S, Se, and Te) for the sensitizers presented in Fig. 1. It is also anticipated that the due to semi-metal effect of Se or Te, the proposed materials would exhibit superior optical and electronic characteristics over oxygen and sulfur-containing dyes.

Computational Details

The geometrical, optical, and electronic properties were obtained using density functional theory (DFT) and time-dependent density functional theory (TD-DFT) methods as implemented in Gaussian 9 [26]. Geometry optimization was performed using B3LYP functional [27] coupled with 6–31 + G(d,p) basis set for light atoms and LANL2DZ basis set for heavy atoms (Se and Te). Next, frequency calculations were perfumed and the absence of imaginary frequencies confirmed that the optimized geometries correspond to the minima on the potential energy surface. Furthermore, simulation of absorption spectra was performed using CAM-B3LYP using the same basis sets for corresponding atoms for optimization and frequency calculations. The simulated maximum absorption was found to be 545 nm which is comparable to the experimental value (546 nm). The dichloromethane solvent was chosen for the simulation of electronic spectra within the polarized continuum model (PCM) as the same solvent was used for the experimental UV-vis spectra measurements on the WS − S molecule.

Adsorption of dyes on the TiO_2 surface was carried out, the conjugate − gradient optimizations were employed using the Perdew − Burke − Ernzerhof (PBE) with the generalized gradient − correlated approximation (GGA) method and the projector augmented plane − wave (PAW) pseudopotentials [28]. The energy cutoff was set at 400 eV for all the adsorption calculations. The convergence threshold for self − consistent iteration was set to 10^{-4}. To consider the van der Waals interactions, the DFT − D3 model [29] was performed. As well, on − site Coulombic repulsion (U) was taken into account by setting U_{eff} = 8.5 eV for Ti atoms [30–34]. The Gamm point in the reciprocal space was used in the geometric relaxation process to reduce the computation consumption. The titanium dioxide (TiO_2) anatase (101)

with 4 · 5 supercell was chosen in this study. The adsorption energy of single dyes on TiO_2 surface was calculated using the equation:

$$E_{\mathrm{ads}} = E_{\mathrm{dye@TiO_2}} - E_{\mathrm{dye}} - E_{\mathrm{TiO_2}}$$

1

where $E_{\mathrm{dye@TiO_2}}$ is the total energy of the adsorbed dyes on TiO_2, $E_{\mathrm{TiO_2}}$ is the total energy of the TiO_2 pure surface, E_{dye} is the total energy of the isolated optimized adsorbate. All adsorption calculations were carried out using the Vienna ab initio simulation package (VASP) [35, 36].

Results And Discussion

Geometrical Properties

The optimized geometries of the 2D molecular structures (Fig. 1) are presented in Fig. 2. The structures' planarity were observed from benzothiadiazole (BTZ) towards cyanoacrylic acid anchoring group this character is beneficial for intramolecular charge transfer and the remaining part induces non-planarity and is important for the reduction of dye aggregation. The measured bond lengths $\delta_{\mathrm{N-X}}$ (2.800 – 2.925 Å) and $\delta_{\mathrm{H-X}}$ (2.486 – 3.099 Å) for optimized structures the bonds strengthen as electronegativity of the chalcogen atom increases.

This observation was similar to the findings by Ortiz-Rodríguez and co-workers where it was observed that the bond length decreases with orbital size mismatch between the chalcogen and the H [37]. These substitutions showed minimal effect on the dihedral angle X – C–C – X which remained ∼180° which implies that the substituted chalcogens did not alter the planarity of the investigated sensitizers. For each chalcogen, the bond and angles θ_1 and θ_2 are equivalent (i.e. $\Delta\theta \approx 0$), however, the values decreased with increasing chalcogen size.

Table 1
The calculated dihedral angle Φ (°), the bond angle $\theta_{i=1\&2}$ (°) and bond lengths δ_i (Å)

	Φ	1	1	$\delta_{\mathrm{N-X}}$	$\delta_{\mathrm{H-X}}$	Mulliken charges	
WS – O	179	108	108	2.800	2.486	−0.321	−0.268
WS – S	179	92	92	2.896	2.799	−0.095	−0.175
WS – Se	178	87	87	2.914	2.930	+ 0.569	+ 0.641
WS – Te	179	82	82	2.925	3.099	+ 0.766	+ 0.852

Mulliken charges on the chalcogenides show that O (− 0.294) carries a strongly negative charge followed by S (− 0.135) in the dyes, while the heavier chalcogens have even positive charges Se (0.605) and Te (0.809). The calculated Mulliken charges demonstrate that Se and Te substituted dyes are more stable than the O and S-substituted dyes, this observation is in agreement with the literature [38].

Optical Spectra

The electronic absorption spectra and emission spectra for the dyes containing heteroatoms (O, S, Se and Te) in the π-linkers are presented in Fig. 3. Furthermore, electronic transitions, maxima absorption, oscillator strength, excited-state lifetime, light-harvesting efficiency and corresponding molecular orbital contributions are shown in Table 2. Both absorption and emission spectra are red-shifted with an increase in chalcogenides atomic size. The absorption spectra were characterized by a dual-band absorption profile, the higher energy bands were observed at around 300 nm and the lower energy bands were found within 500 to 600 nm. Contrary to the lower energy bands, the higher energy bands are nearly equivalent in intensities and positions for all dyes. A noticeable trend was observed in the optical gap among the investigated dyes where WS-O (2.37 eV) exhibited the widest gap, followed by WS-S (2.28 eV), WS-Se (2.16 eV), and WS-Te (2.07 eV) which had the narrowest gap, thus these dyes can absorb light up to 523 nm, 545 nm, 575 nm, and 600 nm, respectively. The optical gap energies of the chalcogenides sensitizers decreased systematically as the chalcogenides varied from sulfur (S) through selenium (Se) to tellurium (Te) where a more pronounced red-shift was observed for dyes containing large-size chalcogen atom. The observed hyperchromic response was consistent with the electronegativity of dopant chalcogen atoms. A similar trend was observed for emission $_{\mathrm{em}} =$ 1.78, 1.67. 1.53 and 1.45 (all in eV); the stoke-shift was found to be 172 (O), 197 (S), 234 (Se), 253 nm (Te). Due to long trailed absorption, red-shifted emission peaks, and larger Stoke's shift (higher than 100 nm) doping with heavy chalcogen may permit simultaneous excitation of different fluorescence colour through a single excitation source; thus, materials containing these elements may be integrated into the building allowing multi-purpose operation.

The maxima absorption band was characterized by HOMO to LUMO as the main electronic transition followed by HOMO − 1 to LUMO, the percentage contributions increase with the increase in the atomic size of the chalcogen atom size where HOMO to LUMO transitions can be found within 55–56% and 32–35% for HOMO − 1 to LUMO transitions.

The intramolecular charge transfer of the studied dyes was assessed through the charge density distribution as depicted in Fig. 4. As can be seen from the figures, the HOMO electron density was mainly delocalized of the donor part extending to benzothiadiazole and only a few traces in one of the modified units. Upon photo-excitation, in the LUMO state, we observe the movement of charge density towards the anchoring group. This phenomenon is evident for intramolecular charge transfer and the investigated sensitizers may efficiently inject charge into the conduction band of the TiO_2 semiconductor.

Table 2
Calculated maximum absorption wavelengths (λ, nm), oscillator strength (f), excited-state lifetime (τ, ns), light-harvesting efficiency (Φ_{LHE}, %), and molecular orbital contributions to the first excited state.

Absorption						
Molecule	**Transition**	**λ**	f	**τ**	**Φ_{LHE}**	**Contributions**
WS − O	$S_0 \rightarrow S_1$	523	2.370	1.73	99.57	H→L(55%); H−1→L(32%)
WS − S	$S_0 \rightarrow S_1$	545	2.273	1.96	99.47	H→L(55%); H−1→L(34%)
WS − Se	$S_0 \rightarrow S_1$	575	2.158	2.30	99.30	H→L(56%); H−1→L(35%)
WS − Te	$S_0 \rightarrow S_1$	600	2.067	2.61	99.14	H→L(57%); H−1→L(35%)
Emission						
WS − O	$S_0 \leftarrow S_1$	695	1.968	3.68	98.92	H←L(65%); H←L + 1(14%)
WS − S	$S_0 \leftarrow S_1$	742	2.154	3.83	99.30	H←L(66%); H − 1←L + 1(16%)
WS − Se	$S_0 \leftarrow S_1$	809	2.368	4.14	99.57	H←L(66%); H − 1←L(16%)
WS − Te	$S_0 \leftarrow S_1$	853	2.321	4.70	99.52	H←L(66%); H − 1←L(14%)

Light-harvesting Efficiency

The performance of DSSC is measured through incident photon-to-current conversion efficiency (IPCE) expressed as:

$IPCE = \Phi_{LHE} \cdot \Phi_{inj} \cdot \Phi_{CC}$

where Φ_{LHE} is the function of light-harvesting efficiency which accounts for electron density movement related to both optical absorption intensity and available electron transition, Φ_{inj} is the electron injection efficiency, and Φ_{CC} is the charge collection efficiency. The Φ_{LHE} can be expressed as $\Phi_{LHE} = 1 - 10^{-f}$; where *f* is the oscillator strength of the sensitizer corresponding to maxima absorption. The obtained *f* are higher than a unit leading Φ_{LHE} higher than 99% or higher (Table 2), it is worth noting that there was no clear trend in the Φ_{LHE} values.

Excited-state Lifetime

Excited-state lifetimes (τ) for the sensitizers under consideration were evaluated, τ is an important factor that influences the charge transfer. A sensitizer with a longer τ is expected to be more facile for charge

transfer and suppresses recombination consequently leading to reduced energy loss. It is a requirement that charge injection time should be shorter than the excited state decay to the ground state for efficient charge injection before radiative or photochemical reactions occur [39–42]. The τ (ns) of a sensitizer can be calculated by using the following relation [43–48]:

$$= \frac{1.499}{f \times E^2}$$

where Δ*E* is the transition energy in cm^{-1} units of measurements; the first excited-state lifetime corresponds to the lowest excitation energies, mostly from $\mathrm{S}_0 \rightarrow \mathrm{S}_1$. Calculated values are found in the range 1.73 − 2.61 ns in the order WS − O < WS − S < WS − Se < WS − Te. One may hypothesize that the inclusion of less electronegative chalcogens (Se and Te) may lead to the stabilization of the excited state possibly supported by the extended valence shell accompanied by the change in hybridization [49].

HOMO-LUMO Energy Levels

Understanding the energy level of the highest occupied molecular orbital HOMO (E_H) or ground state oxidation potential (GSOP) and LUMO (E_L) is critical to the successful design of sensitizers with improved PCE. The E_H and E_L are sensitive to changes in the chemical structures such as nature and placement of the functional group. Charge injection to the CB of the semiconductor proceeds from the unrelaxed excited-state dye species to the CB of the semiconductor [50, 51], the energy level corresponding to this is known as excited-state oxidation potential (ESOP) and can be calculated as: ESOP = GSOP + Δ*E*, where Δ*E* corresponds to the vertical excitation energy/ optical gap which can be obtained from the TD-DFT calculations. The ability of the dye to inject charge into the CB of a semiconductor can be quantified through the free energy of charge injection (ΔG_{inj}) calculated as $\Delta G_{inj} = E_{CB} - \mathrm{ESOP}$, where E_{CB} is the reduction potential of the CB of the TiO_2 semiconductor. The oxidized dye is regenerated by receiving an electron from the $\mathrm{I}^-/\mathrm{I}_3^-$ electrolyte; dye regeneration is quantified through free energy of dye regeneration (ΔG_{reg}) which can be calculated as: $\Delta G_{reg} = \mathrm{GSOP} - E_{\mathrm{I}^-/\mathrm{I}_3^-}$. The energy level alignment diagram with conduction band of TiO_2 semiconductor − 4.05 eV at pH = 7 [52] and redox potential of iodide/triiodide electrolyte and its value is − 4.8 eV [53]. Table 3 shows the calculated GSOP/E_H, vertical transition energies Δ*E*, energy gap E_g, LUMO, ESOP, ΔG_{inj} and ΔG_{reg}. Generally, we observe nearly similar HOMO energies but the LUMO stabilization (i.e., downward shift) results in the narrowed energy gap.

Table 3
The calculated optical gap ΔE, energy gap E_g, the highest occupied molecular orbital (HOMO) energies, the lowest unoccupied molecular orbital (LUMO) energies, excited-ste oxidation potential (ESOP), free energies of charge injection ΔG_{inj} and free energy of dye regeneration ΔG_{reg} (all values in eV)

Molecule	ΔE	E_g	HOMO/GSOP	LUMO	ESOP	ΔG_{inj}	ΔG_{reg}
WS − O	2.37	1.97	−5.11	−3.14	−2.74	−1.31	−0.31
WS − S	2.28	1.87	−5.11	−3.25	−2.83	−1.22	−0.31
WS − Se	2.16	1.78	−5.12	−3.34	−2.96	−1.09	−0.32
WS − Te	2.07	1.77	−5.10	−3.33	−3.03	−1.02	−0.30

Clear trends were observed in the optical (ΔE) and energy (E_g) gaps between dyes. The studied dyes exhibit ΔE values from 2.07 to 2.37 eV and the E_g between 1.77 to 1.97 eV, we observe a positive correlation between the ΔE and E_g defined by the linear equation: $\Delta E = 1.3576 \cdot E_g - 0.2882$ with $R^2 = 92\%$. The decreased energy gaps for dyes containing larger chalcogen atoms is caused by reduced aromaticity in conjugated five-member rings, despite being easier to polarize and having larger atomic radii (O: 0.73 Å; S: 1.02 Å; Se: 1.16 Å; Te: 1.40 Å) [54], exhibit poor orbital overlap with neighboring carbon due to their larger size; aromaticity of the five-member rings decreases in the following order: Te < Se < S < O [55].

Figure 5 shows a minimal shift in the E_H energies among the investigated dyes ranging between − 5.12 to − 5.10 eV, this observation was consistent with the findings by Planells and co-workers [55]; implying that the dyes have comparable ΔG_{reg} within the range − 0.30 and − 0.32 eV. A strong π* character with electron density fully delocalized over the modified units containing the heteroatom resulted in a deeper shift in the LUMO energy level with an increase in heteroatom size which consequently led resulted in a reduced energy gap. It is interesting to note the monotonic decrease in the ESOP energy level from oxygen to tellurium, this observation is consistent with atomic orbital energies for group VI where the p orbital valence energies increase moving down group VI (from O 2p, S 3p, Se 4p, Te 5p) [56].

Adsorption on the TiO2 surface

For the purpose of understanding the adsorption capability of the four dyes on TiO_2 anatase (1 0 1), geometrical parameters and adsorption energies of adsorbed systems were studied using PBE + U level. It is possible for carboxylic acid groups to be anchored to TiO_2 surface through three modes; mono-dentate, bidentate-chelating, and bi-dentate bridging [59]. In previous theoretical studies, the adsorption of carboxylic acid on TiO_2 by bi-dentate was found to be the more stable mode than the other two modes[60, 61]. The reason for this is the binding distance of bidentate is short, resulting in an increase in electron injection rates. Hence, this study considered the bi-dentate bridging mode. Figure 11 presents the optimized geometries of four dyes adsorbed systems.

Using Eq. 1, the adsorption energy (E_{ads})can be determined for the four adsorbed systems and they are tabulated in Table 4 along with geometrical parameters (bond lengths and dihedral angles) using PBE + U functional. Each of the four dyes is adsorbed on TiO_2 by bonded between oxygen atoms of the anchoring group and surface atoms and the bond lengths fall in the range of 2.031–2.122 Å. Based on the literature [62], those values indicated strong interactions between the investigated dyes and the surface.

Table 4

Ti–O bond lengths (Å) dihedral angles (°), adsorption energies E_{ads}, and enegy fermi E_f (eV) for the adsorption systems.

System	$(Ti-O)_1$	$(Ti-O)_2$	[a]ϕ_1	[a]ϕ_2	E_{ads}	E_f
WS – O@TiO_2	2.122	2.084	172.832	175.555	−0.08	−2.60
WS – S@TiO_2	2.044	2.073	171.617	174.275	−0.59	−2.57
WS – Se@TiO_2	2.040	2.075	171.251	173.972	−0.41	−2.49
WS – Te@TiO_2	2.059	2.031	170.866	172.688	−0.77	−2.47
[a] $\phi 1$ $(Ti-O-C-C)_1$; $\phi 2$ $(Ti-O-C-C)_2$.						

The four investigated adsorption systems are stable based on their negative adsorption energies which indicated the exothermic processes occurred. It can be noted also the adsorption energies are relatively small and ranged from − 0.08 to − 0.77 eV. This means it is possible that dyes will be physically absorbed onto TiO_2 surface. Among the four adsorbed systems, WS – Te@TiO_2 has the strongest interaction with the TiO_2 surface due to its higher adsorption energy (the most negative value) leading to faster charge transfer rates and enhanced DSSC performances [62, 63]. The opposite note has been observed for WS – O@TiO_2. On the other hand, the Fermi energies are negative and they increase with increased electronegative of chalcogenides (i.e. from Te to O atoms) in the order WS – Te@TiO_2 < WS – Se@TiO_2 < WS – S@TiO_2 < WS – O@TiO_2. Generally, these results indicated that the dyes were tightly adsorbed on the semiconductor surface, which might result in improved photovoltaic performance.

Conclusion

In the present study, we have reported the optoelectronic properties of dyes featuring five-membered rings π-linkers containing chalcogenides (O, S, Se, and Te). It was observed that the chalcogenides π-linkers affect both geometrical and optoelectronic properties. On the other hand, the absorption and emission spectra are red-shifted in the order of increasing heteroatom size (O < S < Se < Te). The red-shifted absorption between 523 nm to 600 nm resulted in a narrowed energy gap (E_g < 2 eV), this observation

was consistent with decreasing electronegativity of chalcogenides. The studied sensitizers have comparable HOMO energy levels which implies that the dyes may have comparable regeneration ability, there is a down-shift in the LUMO energy level from oxygen to tellurium-containing dyes, this observation is due to the increased atomic orbital energies for the group in the order: O > S > Se > Te. There is the stabilization of the excite-state with an increase in chalcogen atomic size, the evaluated excited-state lifetime are 1.73, 1.96, 2.30, and 2.61 ns for oxygen, sulfur, selenium, and tellurium-containing dyes, respectively. Our evaluation of the reported properties shows that consideration of heavier chalcogen atoms (Se and Te) in sensitizers improves the characteristics of interest; therefore, sensitizers containing chalcogenides could be a key in accelerating power conversion efficiencies for DSSCs enabling renewable energy transformation and future technological advances.

Declarations

Funding

This research received no specific grant from any funding agency in the public, commercial, or not-for-profit sector.

Author contributions

All authors contributed to the study conception and design. Material preparation, validation, formal analysis, writing -original draft were performed by Geradius Deogratias, data collection, analysis, writing –review & editing were performed by Ohoud S. Al–Qurashi and Nuha Wazzan. All authors read and approved the final manuscript.

Conflict of interest

The authors declare that they have no known competing financial interests or personal relationships that could have appeared to influence the work reported in this paper.

Availability of data and material

Materials will be available on request.

Code availability

Not applicable.

Acknowledgement

O. Al-Qurashi and N. Wazzan acknowledge King Abdulaziz University’s High-Performance Computing Centre (Aziz Supercomputer) (http://hpc.kau.edu.sa) for supporting the computation for the work described in this paper.

References

1. Yahya, M., et al., *Organic/metal-organic photosensitizers for dye-sensitized solar cells (DSSC): Recent developments, new trends, and future perceptions*. Dyes and Pigments, 2021. **192**: p. 109227.
2. Hug, H., et al., *Biophotovoltaics: Natural pigments in dye-sensitized solar cells*. Applied Energy, 2014. **115**: p. 216–225.
3. Lee, Y.-H., et al., *Wearable Textile Battery Rechargeable by Solar Energy*. Nano Letters, 2013. **13**(11): p. 5753–5761.
4. Fu, Y., et al., *Integrated power fiber for energy conversion and storage*. Energy & Environmental Science, 2013. **6**(3): p. 805–812.
5. O'Regan, B. and M. Grätzel, *A low-cost, high-efficiency solar cell based on dye-sensitized colloidal TiO_2 films*. nature, 1991. **353**(6346): p. 737–740.
6. El Mouhi, R., et al., *DFT, DFTB and TD-DFT theoretical investigations of π-conjugated molecules based on thieno[2,3-b] indole for dye-sensitized solar cell applications*. Physica B: Condensed Matter, 2022. **636**: p. 413850.
7. Zhang, J., et al., *Flexible Platinum-Free Fiber-Shaped Dye Sensitized Solar Cell with 10.28% Efficiency*. ACS Applied Energy Materials, 2019. **2**(4): p. 2870–2877.
8. Kakiage, K., et al., *Highly-efficient dye-sensitized solar cells with collaborative sensitization by silyl-anchor and carboxy-anchor dyes*. Chemical Communications, 2015. **51**(88): p. 15894–15897.
9. Cui, Y., et al., *Organic photovoltaic cell with 17% efficiency and superior processability*. National Science Review, 2019. **7**(7): p. 1239–1246.
10. Schnappinger, T., et al., *Intersystem Crossing as a Key Component of the Nonadiabatic Relaxation Dynamics of Bithiophene and Terthiophene*. Journal of Chemical Theory and Computation, 2018. **14**(9): p. 4530–4540.
11. Becker, R.S., et al., *Comprehensive Evaluation of the Absorption, Photophysical, Energy Transfer, Structural, and Theoretical Properties of α-Oligothiophenes with One to Seven Rings*. The Journal of Physical Chemistry, 1996. **100**(48): p. 18683–18695.
12. Rossi, R., et al., *Singlet—triplet intersystem crossing in 2,2':5',2"-terthiophene and some of its derivatives*. Journal of Photochemistry and Photobiology A: Chemistry, 1993. **70**(1): p. 59–67.
13. Paa, W., et al., *Femtosecond time-resolved measurements of terthiophene: fast singlet–triplet intersystem crossing*. Chemical Physics Letters, 1998. **292**(4): p. 607–614.
14. Lin, J.B., et al., *Torsional Barriers to Rotation and Planarization in Heterocyclic Oligomers of Value in Organic Electronics*. Journal of Chemical Theory and Computation, 2017. **13**(11): p. 5624–5638.
15. Zhu, H., et al., *Insight into Benzothiadiazole Acceptor in D–A − π–A Configuration on Photovoltaic Performances of Dye-Sensitized Solar Cells*. ACS Sustainable Chemistry & Engineering, 2014. **2**(4): p. 1026–1034.
16. Boutaiba, F., A. Zaoui, and M. Ferhat, *Fundamental and transport properties of ZnX, CdX and HgX (X = S, Se, Te) compounds*. Superlattices and Microstructures, 2009. **46**(6): p. 823–832.

17. Gopal, P., et al., *Improved predictions of the physical properties of Zn-and Cd-based wide band-gap semiconductors: A validation of the ACBN0 functional*. Physical Review B, 2015. **91**(24): p. 245202.
18. Al-Shakban, M., et al., *Novel Xanthate Complexes for the Size-Controlled Synthesis of Copper Sulfide Nanorods*. Inorganic Chemistry, 2017. **56**(15): p. 9247–9254.
19. Mahé, L., S.F. Boughdiri, and J.-C. Barthelat, *Electronic Structures and Energetics in the CuX and Cu2X Series (X = O, S, Se, Te, Po)*. The Journal of Physical Chemistry A, 1997. **101**(23): p. 4224–4230.
20. Maneeprakorn, W., M.A. Malik, and P. O'Brien, *The preparation of cobalt phosphide and cobalt chalcogenide (CoX, X = S, Se) nanoparticles from single source precursors*. Journal of Materials Chemistry, 2010. **20**(12): p. 2329–2335.
21. Ding, J., et al., *Thermoelectric transport properties in chalcogenides ZnX (X = S, Se): From the role of electron-phonon couplings*. Journal of Materiomics, 2021. **7**(2): p. 310–319.
22. Schorr, S., et al., *Crystal structure and cation distribution in the solid solution series 2 (ZnX)–CuInX2 (X = S, Se, Te)*. Journal of Physics and Chemistry of Solids, 2005. **66**(11): p. 1961–1965.
23. Deogratias, G., et al., *Effects of heteroatoms in π-conjugated linkers on the optical and electronic properties of modified triphenylamine based dyes: towards DSSCs' applications*. Journal of Molecular Modeling, 2020. **26**(10): p. 288.
24. Kirenga, P., et al., *Influence of Heteroatoms on the Optoelectronic Properties of Triphenylamine-based Dyes for DSSCs Application: A Computational Approach.* Computational and Theoretical Chemistry, 2022: p. 113644.
25. Deogratias, G., et al., *Effect of substituent in the acceptor on optical and electronic properties of triphenylamine based dyes: A density functional theory/time-dependent density functional theory investigation*. Materials Science in Semiconductor Processing, 2022. **150**: p. 106935.
26. Frisch, M., et al., *Gaussian 09; Gaussian, Inc.* Wallingford, CT, 2009. **32**: p. 5648–5652.
27. Becke, A.D., *Density-functional thermochemistry. IV. A new dynamical correlation functional and implications for exact-exchange mixing*. The Journal of chemical physics, 1996. **104**(3): p. 1040–1046.
28. Perdew, J.P., K. Burke, and M. Ernzerhof, *Generalized gradient approximation made simple*. Physical review letters, 1996. **77**(18): p. 3865.
29. Grimme, S., S. Ehrlich, and L. Goerigk, *Effect of the damping function in dispersion corrected density functional theory*. Journal of computational chemistry, 2011. **32**(7): p. 1456–1465.
30. Liu, Q.-L., Z.-Y. Zhao, and Q.-J. Liu, *Analysis of sulfur modification mechanism for anatase and rutile TiO 2 by different doping modes based on GGA + U calculations*. RSC Advances, 2014. **4**(61): p. 32100–32107.
31. Saranya, G., et al., *Roles of Chenodeoxycholic Acid Coadsorbent in Anthracene-Based Dye-Sensitized Solar Cells: A Density Functional Theory Study*. The Journal of Physical Chemistry C, 2018. **122**(41): p. 23280–23287.

32. Liu, Q.-L., Z.-Y. Zhao, and Q.-J. Liu, *Analysis of sulfur modification mechanism for anatase and rutile TiO2 by different doping modes based on GGA + U calculations*. RSC Advances, 2014. **4**(61): p. 32100–32107.
33. Deogratias, G., et al., *Investigation of optoelectronic properties of triphenylamine-based dyes featuring heterocyclic anchoring groups for DSSCs' applications: a theoretical study*. Structural Chemistry, 2020. **31**(6): p. 2451–2461.
34. Al-Qurashi, O.S., A. Jedidi, and N. Wazzan, *Single- and co-sensitization of triphenylamine-based and asymmetrical squaraine dyes on the anatase (001) surface for DSSC applications: Periodic DFT calculations*. Journal of Molecular Graphics and Modelling, 2021. **104**: p. 107833.
35. Kresse, G. and J. Furthmüller, *Efficiency of ab-initio total energy calculations for metals and semiconductors using a plane-wave basis set*. Computational Materials Science, 1996. **6**(1): p. 15–50.
36. Kresse, G. and J. Hafner, *Ab initio molecular-dynamics simulation of the liquid-metal–amorphous-semiconductor transition in germanium*. Physical Review B, 1994. **49**(20): p. 14251–14269.
37. Ortiz-Rodríguez, J.C., et al., *Stabilizing Hydrogen Adsorption through Theory-Guided Chalcogen Substitution in Chevrel-Phase Mo6X8 (X = S, Se, Te) Electrocatalysts*. ACS Applied Materials & Interfaces, 2020. **12**(32): p. 35995–36003.
38. Marchand, C.M., et al., *Structure and Stability of Y-Conjugated Silylium Cations [Si(XH)3]+ (X = O, S, Se, and Te)*. Journal of the American Chemical Society, 1997. **119**(45): p. 11078–11085.
39. Arunkumar, A., S. Shanavas, and P.M. Anbarasan, *First-principles study of efficient phenothiazine-based D–π–A organic sensitizers with various spacers for DSSCs*. Journal of Computational Electronics, 2018. **17**(4): p. 1410–1420.
40. Deogratias, G., et al., *Tuning optoelectronic properties of triphenylamine based dyes through variation of pi-conjugated units and anchoring groups: A DFT/TD-DFT investigation*. Journal of Molecular Graphics and Modelling, 2020. **94**: p. 107480.
41. Listorti, A., B. O'Regan, and J.R. Durrant, *Electron Transfer Dynamics in Dye-Sensitized Solar Cells*. Chemistry of Materials, 2011. **23**(15): p. 3381–3399.
42. Hardin, B.E., H.J. Snaith, and M.D. McGehee, *The renaissance of dye-sensitized solar cells*. Nature Photonics, 2012. **6**(3): p. 162–169.
43. Gélinas, S., et al., *Ultrafast Long-Range Charge Separation in Organic Semiconductor Photovoltaic Diodes*. Science, 2014. **343**(6170): p. 512–516.
44. Xu, Y., et al., *Theoretical study of high-efficiency organic dyes with the introduction of different auxiliary heterocyclic acceptors based on IQ1 toward dye-sensitized solar cells*. Journal of Molecular Graphics and Modelling, 2019. **86**: p. 170–178.
45. Bourouina, A. and M. Rekis, *Comparison in optoelectronic properties of triphenylamine-imidazole or imidazole as donor for dye-sensitized solar cell: theoretical approach*. Journal of Molecular Modeling, 2021. **27**(8): p. 225.

46. Li, Y., et al., *D-A-π-A based organic dyes for efficient DSSCs: A theoretical study on the role of π-spacer*. Computational Materials Science, 2019. **161**: p. 163–176.
47. Saad Ebied, M., et al., *Effect of carboxylic acid and cyanoacrylic acid as anchoring groups on Coumarin 6 dye for dye-sensitized solar cells: DFT and TD-DFT study*. Structural Chemistry, 2022.
48. Pakravesh, F., M. Izadyar, and F. Arkan, *Effect of electron donor and acceptor on the photovoltaic properties of organic dyes for efficient dye-sensitized solar cells*. Physica B: Condensed Matter, 2021. **609**: p. 412815.
49. Casado, J., et al., *Hybrid Organic Semiconductors Including Chalcogen Atoms in π-Conjugated Skeletons. Tuning of Optical, Redox, and Vibrational Properties by Heavy Atom Conjugation*. The Journal of Physical Chemistry A, 2006. **110**(23): p. 7422–7430.
50. Benkö, G., et al., *Photoinduced Ultrafast Dye-to-Semiconductor Electron Injection from Nonthermalized and Thermalized Donor States*. Journal of the American Chemical Society, 2002. **124**(3): p. 489–493.
51. Zhu, H., et al., *D–A–π–A featured sensitizers by modification of auxiliary acceptor for preventing "trade-off" effect*. Journal of Materials Chemistry C, 2015. **3**(26): p. 6882–6890.
52. Fujisawa, J.-i., T. Eda, and M. Hanaya, *Comparative study of conduction-band and valence-band edges of TiO2, SrTiO3, and BaTiO3 by ionization potential measurements*. Chemical Physics Letters, 2017. **685**: p. 23–26.
53. Preat, J., A. Hagfeldt, and E.A. Perpète, *Investigation of the photoinduced electron injection processes for p-type triphenylamine-sensitized solar cells*. Energy & Environmental Science, 2011. **4**(11): p. 4537–4549.
54. Kaur, M., et al., *Biochemistry of Nucleic Acids Functionalized with Sulfur, Selenium, and Tellurium: Roles of the Single-Atom Substitution*, in *Biochalcogen Chemistry: The Biological Chemistry of Sulfur, Selenium, and Tellurium*. 2013, American Chemical Society. p. 89–126.
55. Planells, M., B.C. Schroeder, and I. McCulloch, *Effect of Chalcogen Atom Substitution on the Optoelectronic Properties in Cyclopentadithiophene Polymers*. Macromolecules, 2014. **47**(17): p. 5889–5894.
56. Woods-Robinson, R., et al., *Wide Band Gap Chalcogenide Semiconductors*. Chemical Reviews, 2020. **120**(9): p. 4007–4055.
57. Zanjanchi, F. and J. Beheshtian, *Natural pigments in dye-sensitized solar cell (DSSC): a DFT-TDDFT study*. Journal of the Iranian Chemical Society, 2019. **16**(4): p. 795–805.
58. Wei, S., et al., *Theoretical insight into electronic structure and optoelectronic properties of heteroleptic Cu(I)-based complexes for dye-sensitized solar cells*. Materials Chemistry and Physics, 2016. **173**: p. 139–145.
59. Pastore, M. and F. De Angelis, *Modeling materials and processes in dye-sensitized solar cells: understanding the mechanism, improving the efficiency*, in *Multiscale modelling of organic and hybrid photovoltaics*. 2013, Springer. p. 151–236.

60. Chen, P., et al., *High open-circuit voltage solid-state dye-sensitized solar cells with organic dye*. Nano letters, 2009. **9**(6): p. 2487–2492.
61. Pastore, M. and F. De Angelis, *Aggregation of organic dyes on TiO2 in dye-sensitized solar cells models: an ab initio investigation*. ACS nano, 2009. **4**(1): p. 556–562.
62. Prajongtat, P., et al., *Density functional theory study of adsorption geometries and electronic structures of azo-dye-based molecules on anatase TiO2 surface for dye-sensitized solar cell applications*. Journal of Molecular Graphics and Modelling, 2017. **76**: p. 551–561.
63. Fu, Y., et al., *Theoretical screening and design of SM315-based porphyrin dyes for highly efficient dye-sensitized solar cells with near-IR light harvesting*. Dyes and Pigments, 2018. **155**: p. 292–299.

Figures

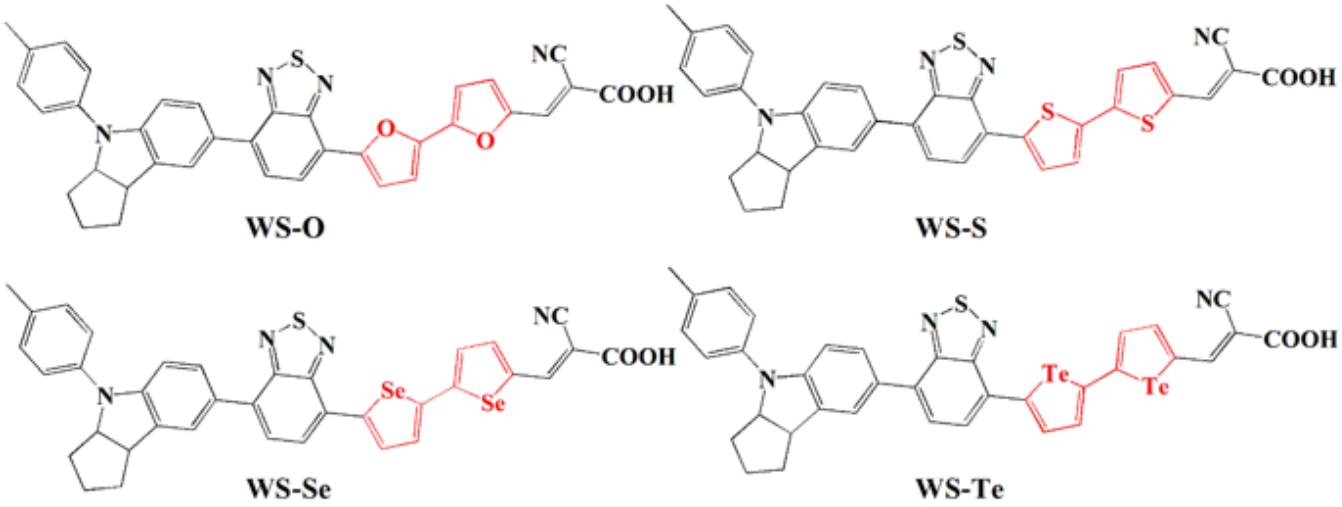

Figure 1

The chemical strucutres of the studied sensitizers containing chalcogenide (O, S, Se and Te) atoms in the p-linkers

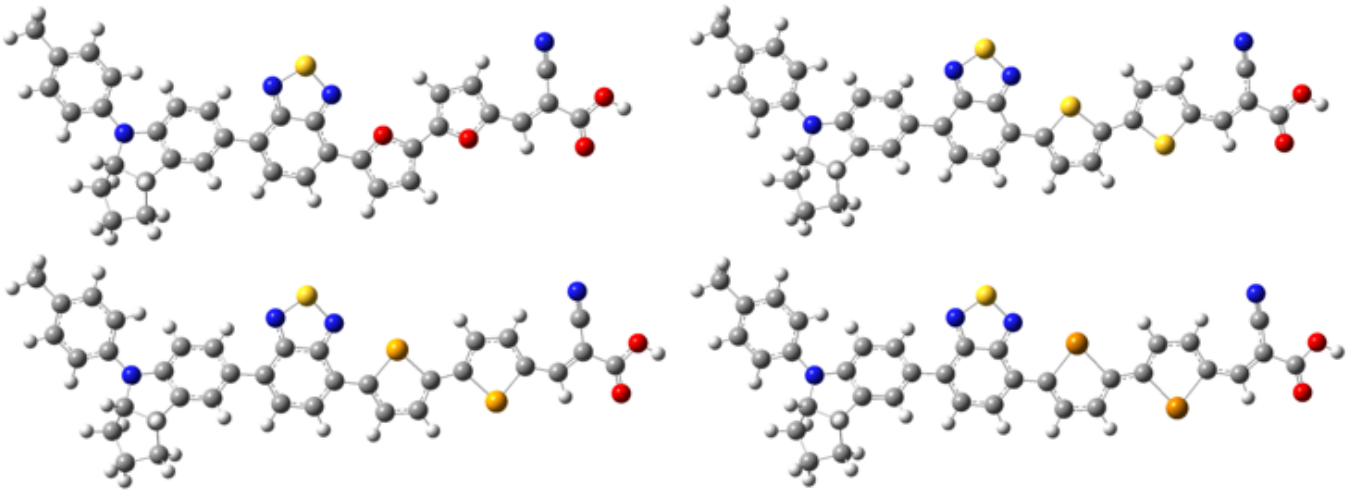

Figure 2

Optimized molecular geometries of dyes containing chalcogenides in the π-linkers

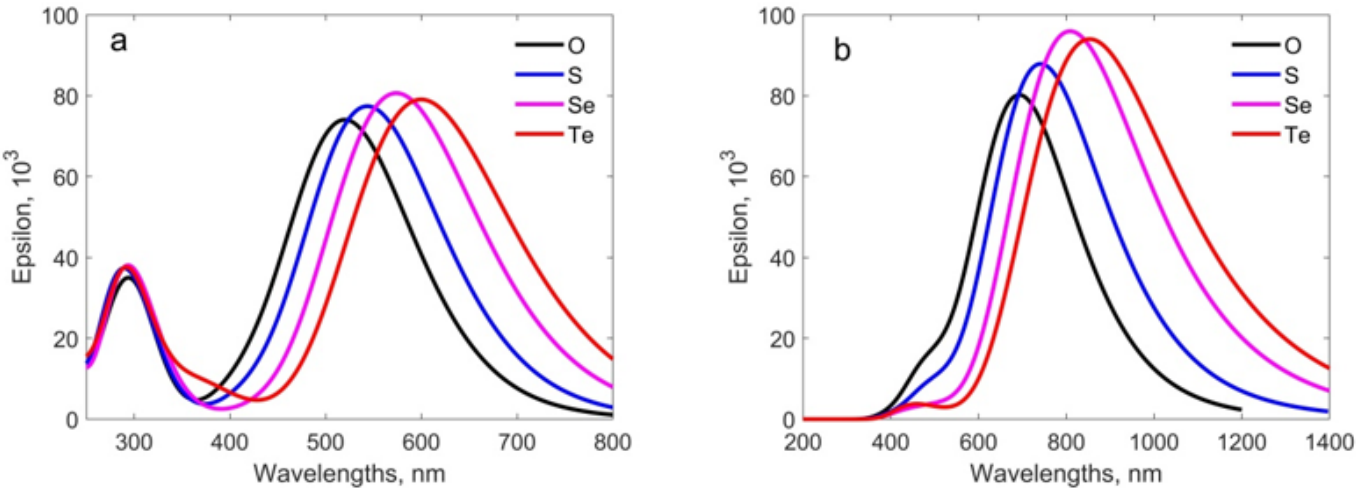

Figure 3

(a) Electronic absorption (b) emission spectra of the investigated dyes containing chalcogenide heteroatoms in dichloromethane solvent

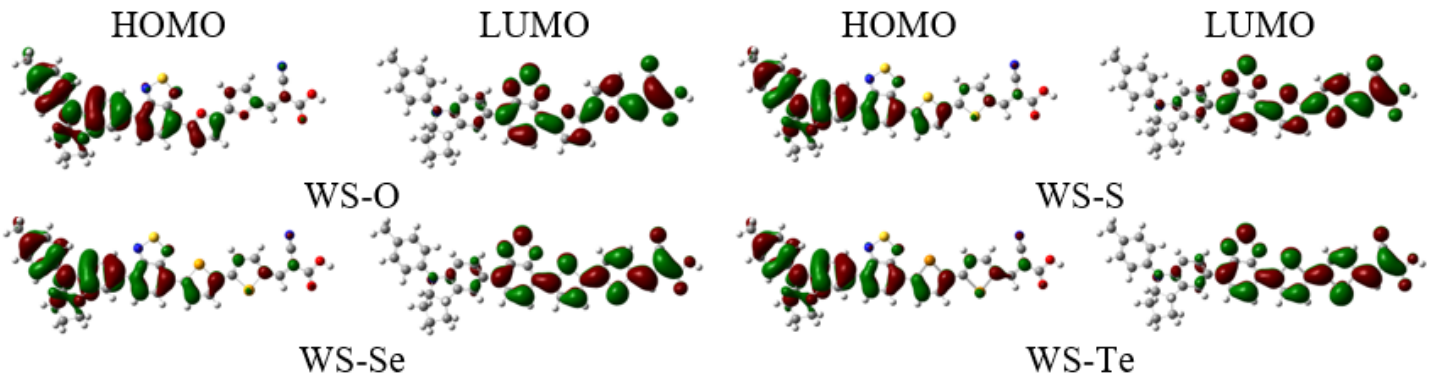

Figure 4

Pictorial representation of charge density distribution for the highest occupied molecular orbital (HOMO) and lowest unoccupied molecular orbital (LUMO) for the investigated sensitizers

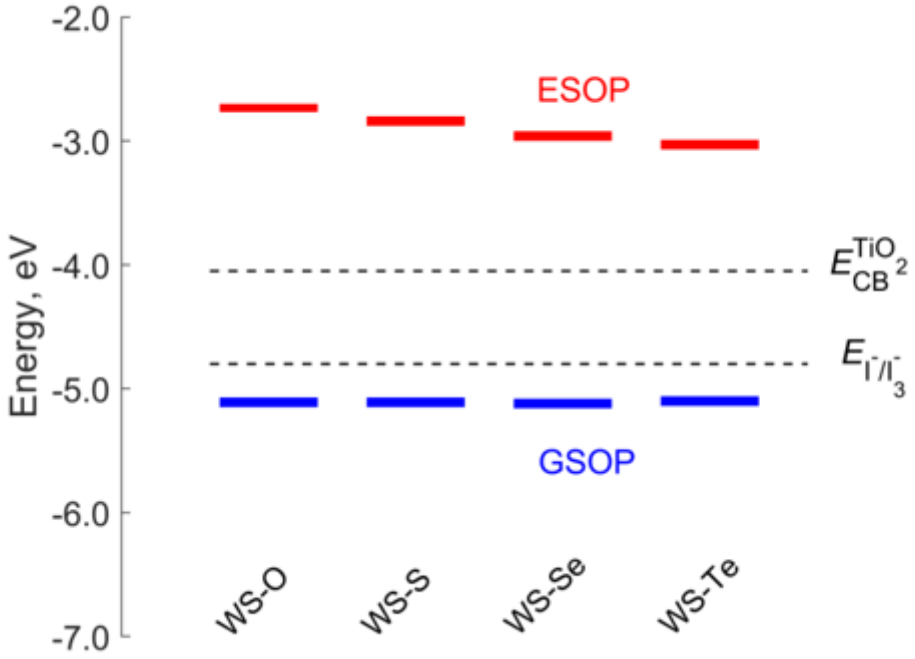

Figure 5

Energy level alignment of the excited-state oxidation potential (ESOP) and ground-state oxidation potential (GSOP) to the conduction band of TiO_2 semiconductor −4.05 eV and redox potential of iodide/triiodide electrolyte −4.8 eV, respectively. Following the order of the ESOP, the absolute value of ΔG_{inj} decreases in the following order WS−O > WS−S > WS−Se > WS−Te, the values are higher than 0.2 eV the minimum requirement [57, 58].

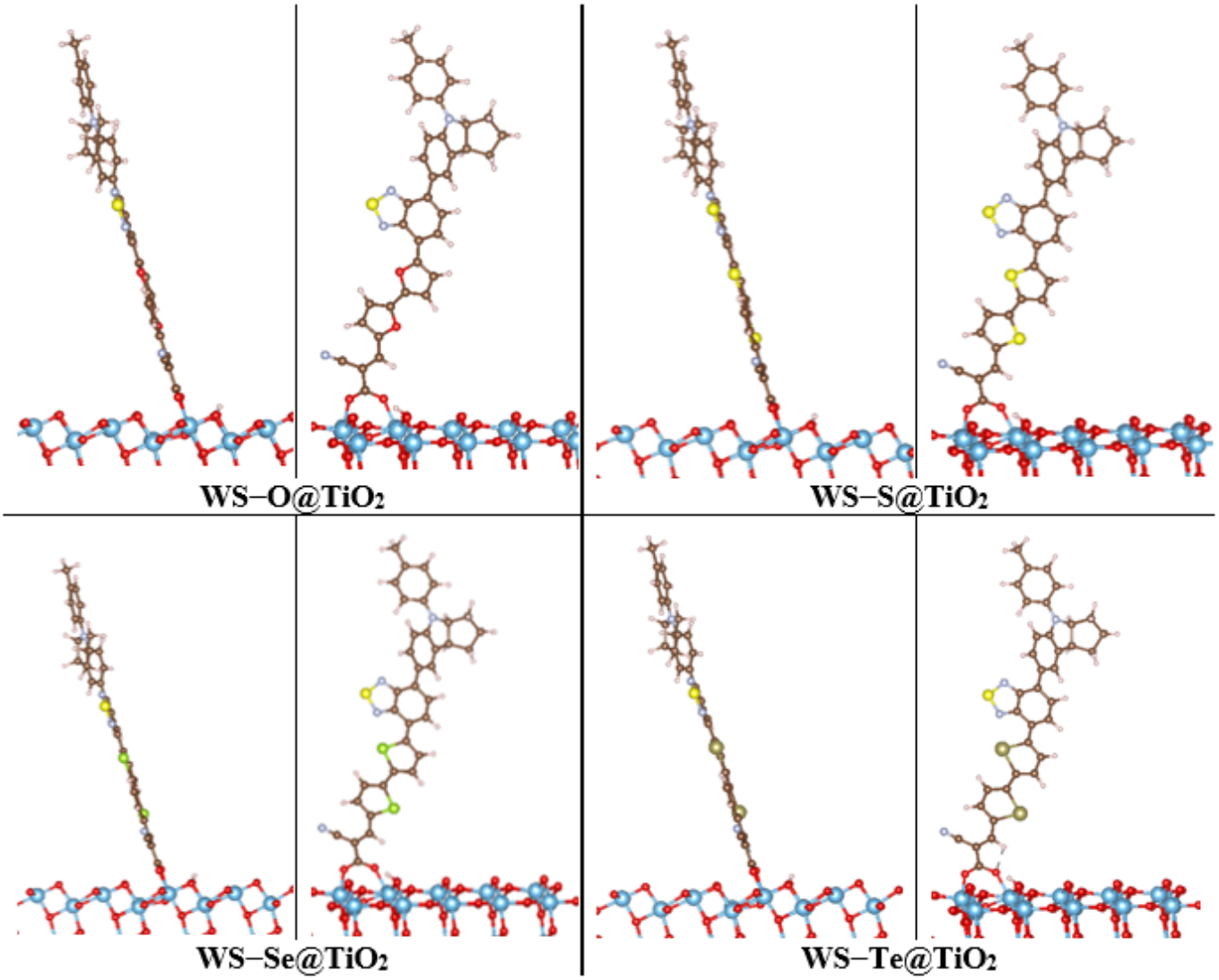

Figure 6

Two orientations of optimized geometries of the four tested dyes on the TiO_2 anatase (101) at PBE+U level. Note: Ti atoms are represented in blue, O in red, C in brown, N in light violet, H in white, S in yellow, Se in light green, and Te in olive color.